

LOW- AND HIGH-FREQUENCY ELASTIC SCATTERING ANALYSIS OF FLUID-FILLED, FLAT-ENDCAPPED CYLINDRICAL SHELLS PROUD ON A SANDY SEABED

ALESSANDRA TESEI, JOHANNES GROEN

NURC

V.le S. Bartolomeo 400, 19126 La Spezia, Italy
tesei@nurc.nato.int

This work presents the analysis of at-sea scattering data by a man-made target which supports the excitation of strong structural waves or resonances, not only at low but even at high frequency ($ka > 100$). The object is a water-filled, flat-endcapped, 2m-long, steel cylindrical shell, measured both at low frequency (2-10 kHz) and at high frequency (120 kHz), where different elastic phenomena are supported and identified. In particular, in the high-frequency sonar images obtained with an AUV-mounted synthetic aperture sonar, significant elastic effects clearly appear, which are interpreted as echoes of a shear wave travelling axially along the cylindrical shell. For interpretation of sonar images it is crucial to understand and predict these supplementary scattering mechanisms.

INTRODUCTION

The state-of-the-art techniques for detection and classification of object lying proud on the seafloor from high-frequency sonar images are generally based on the assumption that the objects of interest are acoustically rigid. With “high frequency” we intend here sonar frequencies for which the dimensionless product of wavenumber k and object radius a exceeds 100. The information from the acoustic images used for detection/classification is extracted in terms of a highlight, coming from reflection/diffraction effects, and a shadow cast on the seabed, both generated by the object’s external shape.

Figure 1(a) shows a typical example of Synthetic Aperture Sonar (SAS) image of a water-filled cylinder proud on a sandy seabed and insonified at oblique incidence by a 300-kHz sonar. The shape and size of the object can be estimated by Automatic Target Recognition (ATR) techniques [1] from the echo scattered by the illuminated part of the object, and from its shadow, both included in the dashed-line box. The sonar data were collected by the MUSCLE Autonomous Underwater Vehicle (AUV) during the COLOSSUS’06 sea trial close to Marina di Carrara, Italy (June 2006). Details about the sonar, the SAS processing and the geometry of the experiment can be found in [2].

If a man-made target is insonified at low- to mid-frequencies, it is well established that it may support the excitation of strong structural waves or resonances consistent with its structural symmetries. As an example, Figure 1(b) shows the image (emphasized by the dashed-line box) of the same cylinder shown in Fig. 1(a) when the object was flush buried in a high-density-clutter sandy seabed. In this case the seabed area was insonified by a parametric sonar in the frequency band 2-15 kHz (roughly corresponding to 2-16 ka) during the GOATS'98 sea trial in Elba Island, Italy [3][4]. The object signature is characterized by the long straight line of the front specular echo followed by sets of parallel straight line features which correspond to the echoes of different acoustic and elastic waves travelling inside the fluid filler and guided by the cylinder shell walls respectively. They are interesting features exploitable for object classification.

This work shows that, under certain conditions, significant elastic scattering phenomena can be excited as well, even at high frequency ($ka > 100$). In particular, the excitation of meridional rays of shell-borne elastic waves is studied here, as they are expected to provide very strong and peculiar features on the sonar images of liquid-filled cylindrical shells. For interpretation of high-frequency sonar images it is crucial to understand and predict these supplementary scattering mechanisms in order not to misinterpret their effects. Similar features were predicted by theory [5][6][7], and their evidence was shown through tank experiments on scaled, canonical-shaped objects (namely small cylindrical tubes) under free field conditions [8]. In this paper they are detected and analyzed on at-sea sonar images of a mine-sized, water-filled, flat-endcapped, steel cylindrical shell sitting on a sandy bottom and measured at between 105 and 135 kHz [9], roughly corresponding to a range of 110-141 ka . The cylinder studied here is 2 m long, has a 0.25 m radius and a 6 mm shell wall thickness.

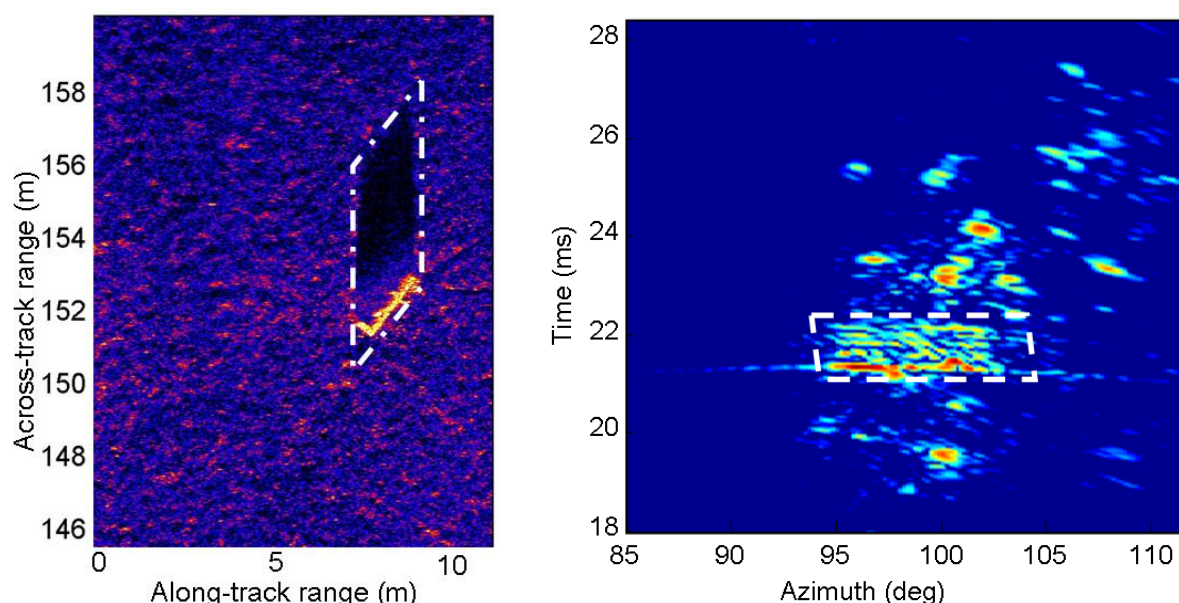


Fig.1 (a) High-frequency (300 kHz) SAS image of a water-filled cylinder proud on a sandy bottom. (b) Low-frequency (2-15 kHz) image of the same water-filled cylinder, flush buried in a high-density-clutter sandy bottom

The same object had been previously measured also at low frequency (2-10 kHz) while it was lying proud on a flat sandy bottom. These data were collected during the MCG'97 sea campaign conducted in the Biodola Bay (Elba Island, Italy) [10]. At low-frequency the

backscatter target signature was dominated by elastic effects around normal incidence. An accurate wave analysis was applied: among the elastic waves excited, one of the most significant contributions was from the shear wave detected also in the high-frequency data.

The paper is organized as follows. Section 1 briefly provides fundamentals on broadband acoustic elastic scattering by fluid-filled cylindrical shells insonified at oblique incidence. Section 2 presents model-data comparison and wave analysis of elastic scattering measurements of the cylinder at low-frequency. Section 3 describes the high-frequency sonar images obtained through SAS processing. The analysis of the high-frequency SAS image of the cylinder characterized by strong elastic effects is presented in Sect. 4, where comparison is provided between experimental data and theoretical predictions. Finally, Section 5 draws some conclusions.

1. ELASTIC WAVES SCATTERED BY CYLINDRICAL SHELLS

The theoretical interpretation of the elastic phenomena observed on liquid-filled, flat-endcapped, finite cylindrical shell assumes that the predicted surface-guided elastic waves have the same dispersion characteristics of waves of the same type supported by an infinite cylinder of the same circular cross-section and material. The phase speed is assumed to be independent of the incident angle [8], at least at frequencies beyond the shell's ring frequency (here estimated at $f_R = 3.3$ kHz [11]). Also, it is assumed that the elastic waves excited in the cylindrical body perfectly reflect at the endcap without any mode conversion. Finally, in the computation of the time of arrival of the different echoes the shell thickness is considered negligible.

If the cylinder is insonified at normal incidence by a plane wave, guided Lamb-type waves of various orders may be supported [12][13]. These waves are launched coherently along the whole length of the cylinder and travel along the cylinder's circular cross-section.

When the object is insonified at an oblique incident angle α with respect to the normal to the cylinder axis, additional purely compressional (P) (expected to be detectable at $ka > 10-15$ only) and shear (T) waves may be supported by the shell [4]. An elastic wave l is launched on the shell at oblique incidence if $0 < \alpha < \theta_c^l$, where θ_c^l is the coupling angle specific of that wave and is defined as $\theta_c^l = \text{asin}(c_{ext}^l / c_{ph}^l)$, with c_{ext} and c_{ph}^l being the sound speed in the loading fluid and the phase speed of the wave l respectively. The travel path of the surface-guided wave is helical. As the incident angle varies, on the (f vs. α) plane the resonance frequencies of the wave l lie on mode loci (one per n) that are computed according to the following expression [4]:

$$\alpha_n^l = \text{asin} \left(\frac{c_{ext}}{c_{ph}^l} \sqrt{1 - (nc_{ph}^l)^2 / (2\pi a f_n^l)^2} \right). \quad (1)$$

The mode loci are quasi-parabolic curves centered at broadside with an asymptote at the wave coupling angle θ_c^l .

When $\alpha = \theta_c^l$ the helical wave l degenerates into a meridional wave: the wave starts to propagate axially (or meridionally) along the longitudinal cross-section of the cylindrical body. These meridional rays are predicted to contribute to the object backscatter with a strong energy enhancement. The enhancement is not only due to end effects but also by the curvature of the shell walls that causes focusing of the part of sound that radiates in the filler [8][14]. Beyond the limit $\alpha = \theta_c^l$ the wave becomes evanescent and does not reradiate in the far field.

If the inside cavity is filled with a liquid, and if the shell walls are thin, there is significant propagation of sound inside the shell. This acoustic energy follows different paths with multiple bounces on the internal shell wall, depending on the angle of incidence on the circular cross-section and on the refraction index M between the external and internal sound speeds ($M = c_{ext}/c_{in}$) [15]. Only sound impinging on internal walls at particular angles (for a specified value of M) will reradiate outside in the backscatter direction. The multiple internal reflections are expected to propagate in the filling medium bouncing on the internal walls at points along helical paths [4]. The strongest contribution is given by the internal bounce of first order, corresponding to sound traveling on the plane of the object cross-section containing the cylinder longitudinal axis.

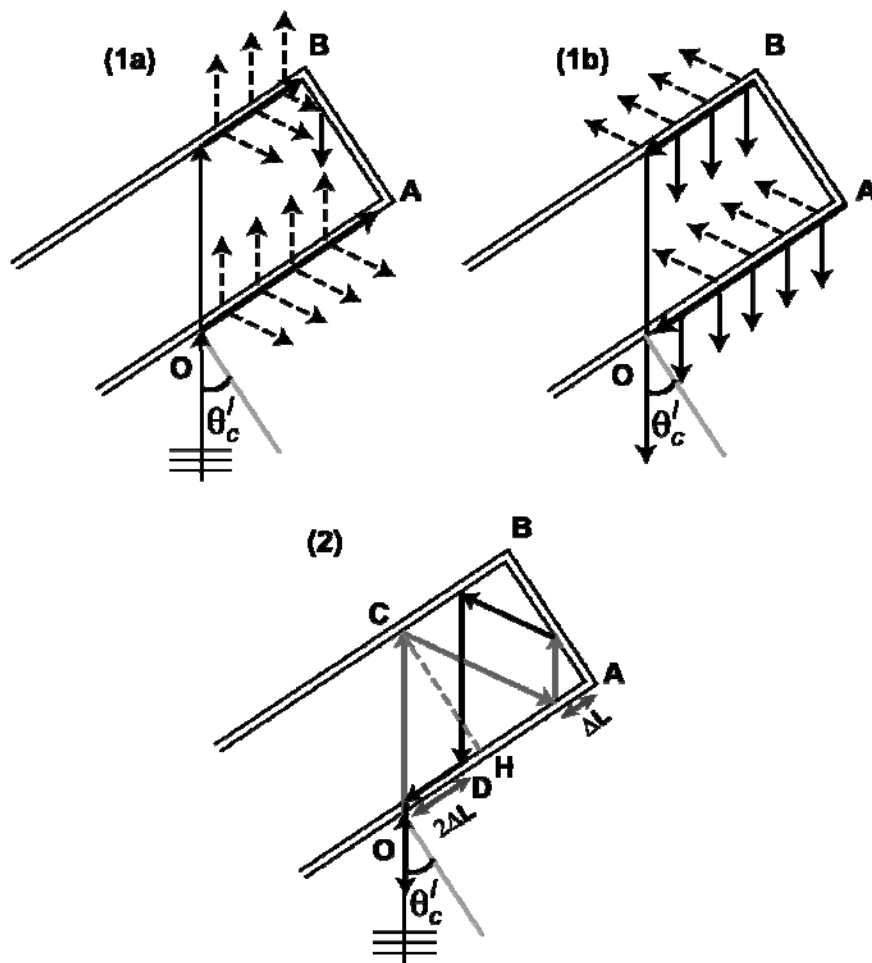


Fig.2 Ray diagram of the propagation of the meridional rays of a surface-guided elastic wave l along a liquid-filled flat-endcapped shell. Examples of possible travel paths that sound launched at point O can follow to make a complete turn before reradiating back to the receiver. (1a) The elastic wave couples onto the shell's front wall, starts to propagate axially along the shell walls while it reradiates both outward and in the filler according to its coupling angle. The radiation into the shell cavity is predicted to cause the excitation of the wave also in the rear wall. (1b) Once reflected by the cylinder ends in A and B, the axial rays propagate along the shell walls in the opposite direction, while reradiating into the interior and exterior media, and, hence, also back to the receiver. The paths of sound scattered back to the receiver are in solid lines. (2) Example of the longest travel path that sound radiated inside the shell by the meridional wave can follow inside the shell cavity; the path before reflection from the endcap is in gray, the path of sound after reflection on the endcap is in black

In this paper, the case of meridional propagation paths of the shell-borne elastic waves is particularly addressed. The time of arrival of the meridional rays (hence the location of their echoes on the sonar image) can be predicted by extending the computation proposed in [8] for a finite cylindrical shell without endcaps to the case of a finite cylindrical shell with flat endcaps. The ray diagrams of Fig. 2 show the travel paths of axial propagation of an elastic, surface-guided wave l on the cross-section of the cylinder containing its longitudinal axis. The curvature effects are neglected. Sound can follow many possible paths before re-radiating back from the launching point, but its time of arrival depends only on the number of times it traverses the cavity [8]. Following the notation in [8], we denote with $sl = 2a / \cos \theta_c^l$ the distance traveled by a meridional ray traversing the cavity (i.e., the segment OC in Fig. 2(2)) and with $sh = 2a \tan \theta_c^l$ the equivalent distance along the shell (corresponding to OD in Fig. 2(2)). While in [8] backscattering could occur only if the launching point was an integer number of times the distance sh , here the presence of the two flat endcaps provides more possibilities of backscattering as sound propagating in the filler can be specularly reflected on the endcap internal face (Fig. 2(2)). With reference to Fig. 2, if the launching point O is displaced $((m + q)sh + \Delta L)$ from the corner A, being m the number of distance intervals sh traveled along the shell, q the number of times a ray traverses the cavity and ΔL the difference between the distance OA and the maximum integer number of sh segments contained in OA, the time the ray takes to make a complete round path from O is:

$$t_{merid,O} = 2 \left(q sl / c_{ext} + (m sh + \Delta L) / c_g^l \right). \quad (2)$$

On the sonar image, the along-track and across-track distances of the meridional ray echo launched from O with respect to the echo from the reference corner A are:

$$\begin{aligned} x_{merid,A} &= ((m + q)sh + \Delta L) \cos \alpha \\ y_{merid,A} &= \left(((m + q)sh + \Delta L) \sin \alpha / c_{ext} - t_{merid,O} \right) c_{ext} / 2 \end{aligned} \quad (3)$$

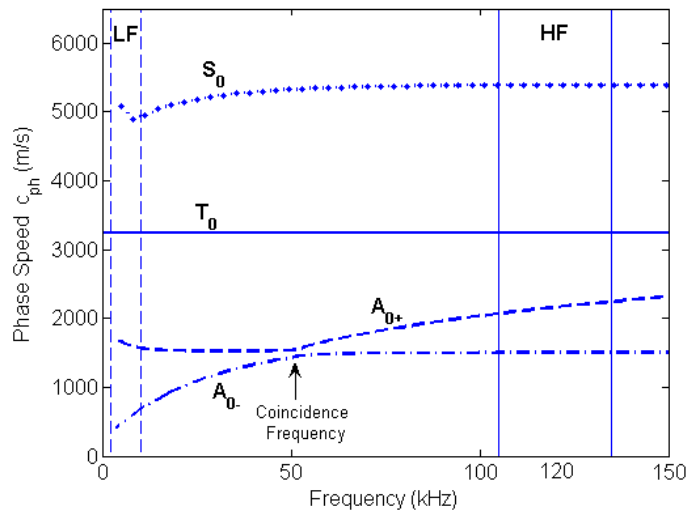


Fig.3 Phase dispersion curves of the elastic waves analytically predicted for a water-filled, infinite, steel cylindrical shell in water (outer radius $a=0.25\text{m}$, wall thickness $d=0.006\text{m}$). They are considered a very good approximation of the phase speeds of the wave supported by a flat-endcapped, 2m-long cylinder of the same nominal size and material. The broad frequency bandwidth includes the studied low-frequency (bounded by the two dashed vertical lines), and high-frequency (solid vertical lines) bands of the sonars used for the at-sea measurements. The dispersion curves of the acoustic multiple internal bounces are omitted

The phase and group speeds of the elastic waves supported by a cylindrical shell come from analytical modal analysis [16] and are used to evaluate the coupling angle of an elastic wave and Eqs. (1) to (3). Figure 3 shows the phase dispersion curves of the elastic waves supported by a water-filled, infinite cylindrical shell having the same nominal radius, shell wall thickness and material properties of the object measured. Steel nominal parameters are compressional speed $c_p=5950$ m/s, shear speed $c_s=3240$ m/s and density $\rho=7700$ kg/m³. From the plot it is possible to identify the types of elastic waves which are excited in the bandwidths of the sonar systems used for either the low-frequency or the high-frequency measurements. The phase speed dispersion curves of the multiple internal bounces are omitted for the sake of readability. The group speed can be easily obtained from the phase speed through the following expression [17]:

$$c_g^l = c_{ph}^l + k^l (\partial c_{ph}^l / \partial k^l), \quad (4)$$

k^l being the wavenumber of the elastic wave.

2. ELASTIC SCATTERING ANALYSIS AT LOW- TO MID-FREQUENCY

A water-filled cylinder was measured proud on a flat sandy bottom by a parametric sonar mounted on a 10m-high tower which could be moved along a rail deployed on the seabed about 40m far from the object, with a resulting incident grazing angle of about 11° [10]. The low grazing angle helped to keep the seabed reverberation low and to reduce the Lloyd mirror effect of interference by the seabed with the object signature [4]. Varying the position of the sonar along the underwater rail allowed the collection of multiple-aspect backscatter data. The incident oblique angle was between 0 and 23°, where 0° corresponds to normal incidence.

Figure 4(a) presents the simulated Target Strength (TS) of the object in the frequency band 2-10 kHz, well below the coincidence frequency [18] of the studied shell, that is predicted around 50 kHz, as one can evaluate from Fig. 3. Simulations come from a (Finite Element Model - Boundary Element Model) FEM-BEM modelling tool assuming the cylinder in the free space [19]. The cylinder scattering is simulated for tilt angle ranging between -90° and 90°, where 0° corresponds to normal incidence. The multiple-aspect measurements of the back target strength is plotted (Fig. 4(b)) together with its mirrored image around broadside. Although the cylinder measured was sitting on a sandy bottom, the Lloyd-mirror effect was relatively weak due to the low grazing angle, and a good agreement could be achieved between the free-field model and the real data. The two images show a regular, patterned texture around broadside aspect. The resonance mode loci of the expected elastic waves were predicted on the basis of the computation of the phase speed dispersion curves of Fig. 3, and by applying Eq. (1). The most evident mode loci are superimposed on the simulated and real data on one half of each image, by leaving the other half for comparison.

Elastic scattering is localized in the aspect angle range roughly between $\pm 27.5^\circ$, which is the critical angle of the shear wave T_0 , namely the lowest-speed supersonic elastic wave for a steel object in water. In particular the shell-borne, helical S_0 Lamb-type and shear T_0 waves are identified and show a very good agreement with the simulation. It can be noticed, particularly in the at-sea data plot (Fig. 4(b)), that also at relatively low frequency, beyond 9 kHz, strong backscatter energy appears around aspects $\pm 23^\circ$ and corresponds to re-radiation of the shear T_0 wave, the resonance mode loci of which will tend asymptotically to its coupling angle $\pm 27.5^\circ$ at higher frequencies. This wave is expected to be excited in a very broad band

and have meridional ray component if the cylinder is insonified in the aspect range of $\pm (27.5 \pm 5)^\circ$ [8].

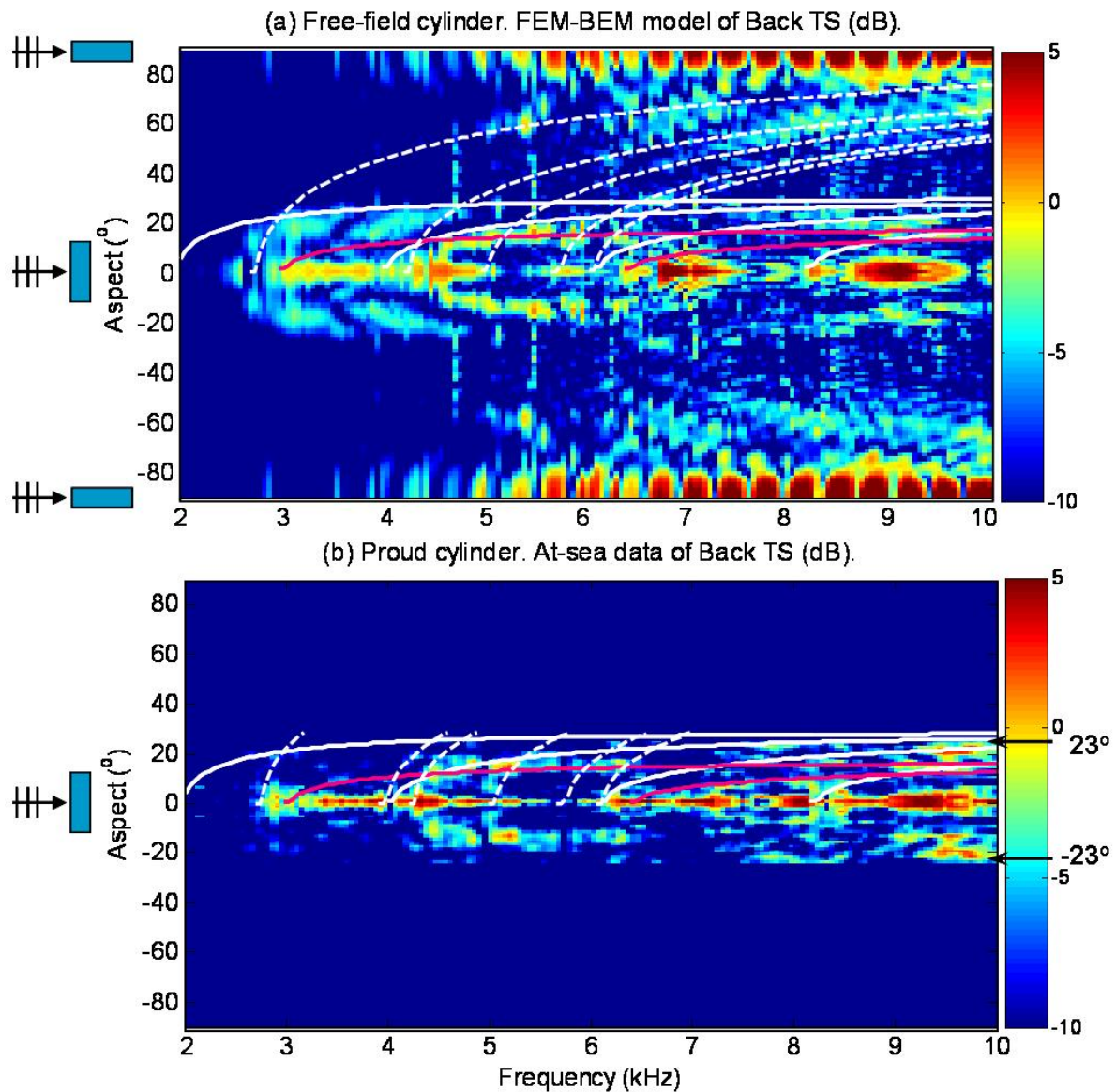


Fig.4 Model-data comparison of low-frequency multiple-aspect measurements of a water-filled cylinder lying proud on the seabed. At-sea data are available only for incidence aspects between 0° (namely normal incidence) and 23° . The back Target Strength (TS) data were mirrored around broadside aspect. The model of the identified resonance mode loci are superimposed on the simulated and real data for positive aspect values. The main resonance mode loci are considered: red-solid lines localize the S_0 Lamb-type wave resonance mode loci, white-solid lines the shear wave mode loci, and white-dashed lines the resonances caused by inner-fluid-borne waves. The second mode of the shear wave is particularly strong and evident off broadside

Beyond the shear wave coupling angle, the signature of the cylinder is characterized either by acoustic waves of diffraction from the external shape of the cylinder, or by multiple internal bounces [4]. Features from internal bounces are partially visible in the data, especially around

broadside. Only the first modes of acoustic multiple internal bounces are shown in the model and data plots, but they are expected to significantly contribute to the backscatter response of the cylinder in a very wide frequency band ranging from few to hundreds of kHz.

3. HIGH-FREQUENCY SONAR DATA AND SAS PROCESSING

The same water-filled cylinder studied in Sect. 3 was measured with the dual sided 8-element Small Synthetic Aperture Minehunter (SSAM) sonar mounted on a REMUS-600 Autonomous Underwater Vehicle (AUV) which was supplied by the Naval Surface Warfare Centre - Panama City (NSWC-PC), and described in [9]. The data were acquired during the MX3 sea trial, jointly conducted with the NATO Undersea Research Centre in a coastal area of the Ligurian Sea near Framura, Italy, in November 2005.

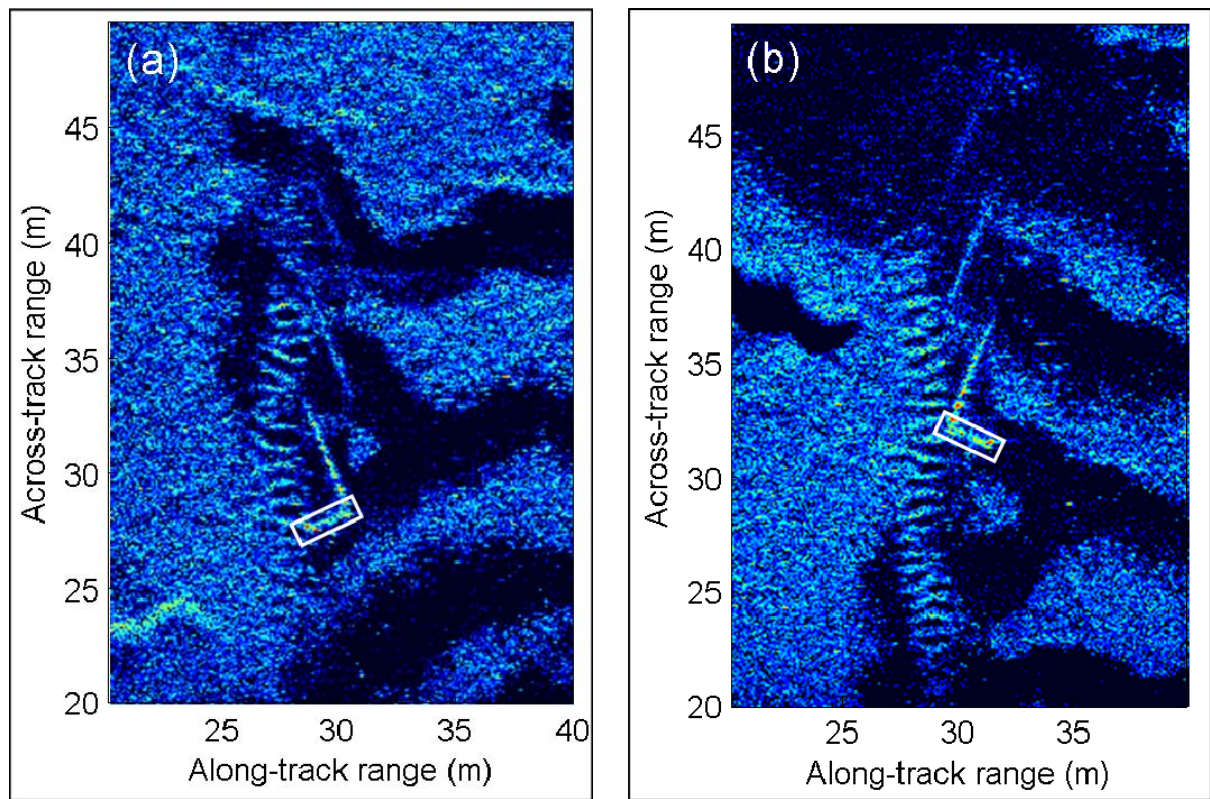


Fig.5 High-frequency SAS images of the water-filled cylinder proud on a sandy seabed. Starboard (a) and port (b) images show the same phenomena. A white box emphasizes the cylinder diffraction echoes on each image

The AUV was run through an area with a complex and highly variable bottom consisting of a combination of mud, sand, rippled sand and Posidonia. A situation like this is a challenge for synthetic aperture sonar, which depends on bottom reverberation being stationary and homogeneous to a certain extent. The search pattern of the AUV was a lawnmower pattern, which resulted in relevant measurements of the cylinder of interest sitting on the sea floor at approximately 30 meters with both the port and starboard sonar during different legs of the mission (Fig. 5). The cylinder was sitting in a sandy flat area at the border of a rippled sandy patch. From the images it is possible to estimate that the cylinder was tilted 23.7° with respect to broadside aspect. Its front echo and shadow are evident, although the

shadow is not valuable as a detection/classification clue in these images due to interference with additional features of the cylinder. These additional features appear as a series of three parallel, straight-line, strong echoes oriented almost perpendicular to the longitudinal axis of the object. The first one of these echoes starts from one of the extremes of the cylinder's diffraction highlight. Both images show the same effect.

3.1 SAS signal processing

The input data for the SAS came from a linear array of eight elements, which were matched filtered with the transmitted signal, a chirp around 120 kHz with a bandwidth of 30 kHz. The ping repetition time of the sonar was adjusted such that two elements were overlapping. This means that the signal on the first element is expected to be the same as the signal on the seventh element of the next ping. When there is a difference, it is assumed to be caused by motion, more specifically by surge and sway, which can both be estimated in this way. This sonar correlation technique called displaced phase centre (DPC) is used in combination with output from heading sensor to estimate the motion of the sonar for the pings needed to build up the synthetic aperture. The data at element level are now imaged in two steps, i.e. with a beamformer and a stacking algorithm. The estimated position for each ping and each element are accounted for in the imaging process, so no assumptions or errors are made here. The resulting image contains acoustic pressure values as a function of range and across-range.

The acoustic pressure in the SAS image is a combined result of all elements of the pings integrated. The bandwidth of the transmitted signal and the length of the synthetic aperture theoretically determine the resolution in the image, which is 25 by 50 mm in this case. The synthetic aperture length increases with range, i.e. a scatterer is present in more pings at longer range, and at a range of 30 m this length is about 3.6 m. Instead of looking at synthetic aperture length it is better to regard the synthetic aperture integration angle β , because it is directly coupled to the across-range resolution and can be seen as spatial wavenumbers. It can be found in [20] that resolution and integration angle are interrelated by

$$4\Delta x_{3\text{dB}} \tan \beta/2 = \lambda, \quad (5)$$

where λ is the centre wavelength of the transmitted signal and $\Delta x_{3\text{dB}}$ is the across-range resolution. An aspect of high interest to this article's analysis is the trade-off visible in this formula. The echoes that are received from the cylinder are expected to be sensitive to aspect angle. We want to analyse the effect at given angle. On the other hand we need resolution, because the target echo needs to be separable from reverberation and other noise sources. We must therefore allow some variation in the view angle. When we fill in the parameters in Eq. (5) we see that the integration angle is around 7° .

4. ELASTIC SCATTERING ANALYSIS AT HIGH-FREQUENCY

The starboard image of Fig. 5(a) is zoomed around the cylinder and its scattering phenomena (Fig. 6). It is possible to distinguish two straight-line echoes along the main axis of the cylinder: the first one is the front echo of diffraction, the following one is the reflection from the rear internal wall of the shell (first-order internal bounce). The additional three strong echoes oriented perpendicularly are interpreted as periodic echoes of a meridional elastic wave.

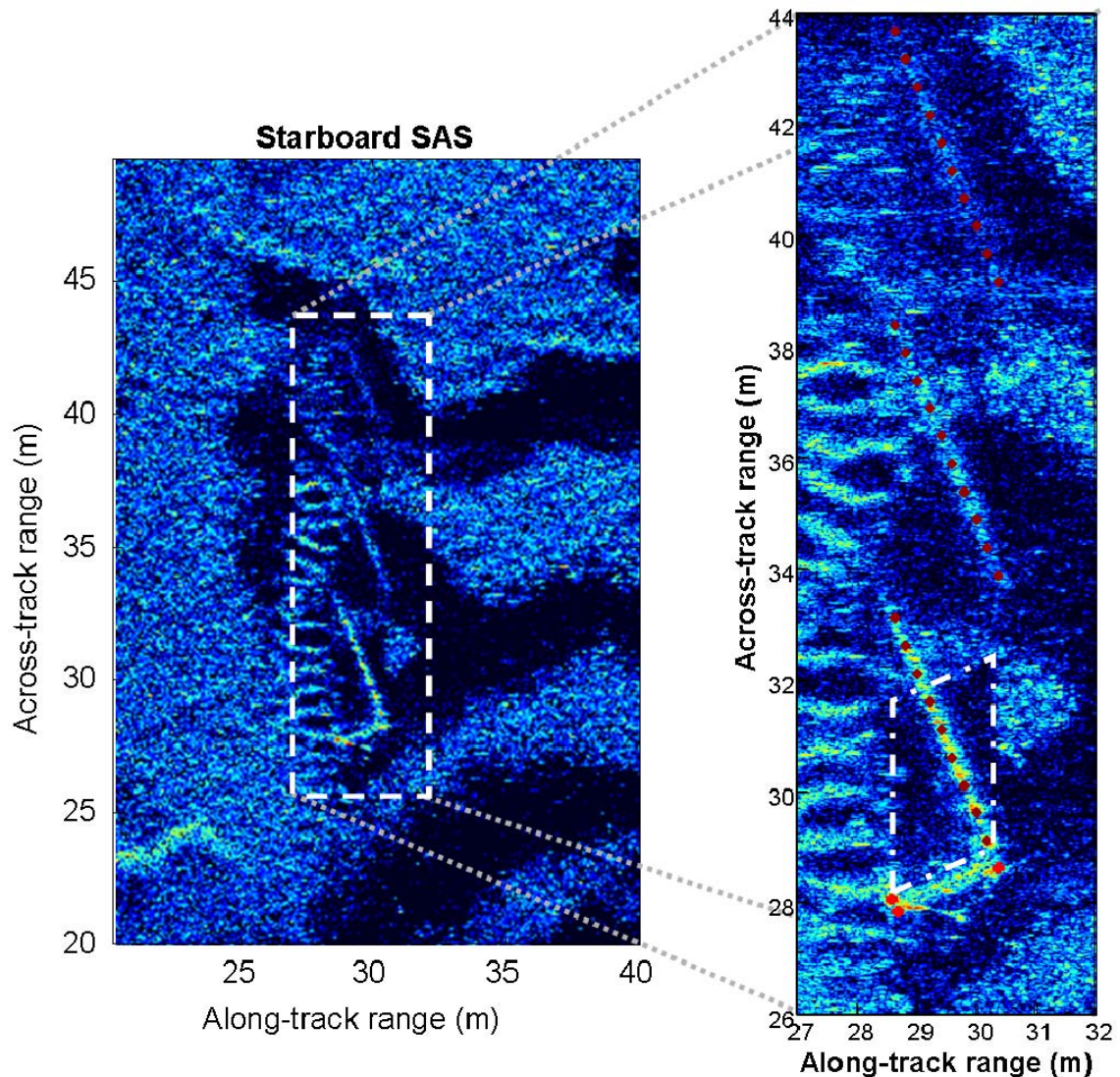


Fig.6 Part of the starboard-SAS image of Fig. 5(a) is bounded by the dashed-line white box and zoomed on the right. The target shadow, bounded by the white-dashed line box, follows the diffraction echoes along the cylinder's longitudinal axis. The light-red dots localize the predicted extremes of the illuminated faces of the cylinder. The dark-red dots emphasize the predicted times of arrival of the periodic echoes of the meridional ray of the shear wave traveling along the shell

Given the estimate of the cylinder tilt angle the wave generating this particular phenomenon of strong scattered echoes should be the shear wave T_0 , the coupling angle of which is predicted to be 27.5° for steel shells, as anticipated in Section 1. The fact that three subsequent echoes of the same wave appear on the SAS image means that the wave could propagate axially along the whole length of the cylinder at least for three times (from one end to the other and then back to the starting point), before being so attenuated as to be undetectable. As material dissipation in steel is practically negligible, energy leakage is only due to radiation damping. The length and orientation of each straight-line echo is in perfect agreement with the prediction: the length of the echoes depends only on the cylinder length if the object is totally contained in the transmit/receive beams, their orientation depends on the

phase speed of the elastic wave causing the particular phenomenon and on the sound speed in the filling liquid.

The effect detected is known to be sensitive to the aspect angle and to the acoustic/elastic properties of the filler. As the studied effects are caused by a spatially coherent radiation of an elastic wave along the whole length of the cylinder, they are particularly enhanced by SAS processing, if the platform stability allows the insonification of the object approximately at the same incident angle (within about 5°). The good platform stability allowed the SAS processing to further enhance the effect due to high resolution and array gain. A relatively wide beam in transmission allowed the complete insonification of the object at each ping, which implies the possibility to launch the meridional rays all along the longitudinal axis of the cylinder, with consequent strong enhancement of the corresponding echoes. Similarly, also a relatively wide receive beam helped to enhance the phenomenon and, in particular, to extend the length of each elastic echo as from theoretical expectations. Furthermore, the presence of the flat endcaps contributed to a stronger backscattering if compared to an open tube of the same size [8].

5. CONCLUSIONS

The presented work showed that elastic scattering phenomena can be excited and can be significant not only at low but even at high frequency ($ka > 100$). In particular, the paper addressed the analysis of meridional rays of shell-borne elastic waves which generated very strong and peculiar features on the sonar images of liquid-filled cylindrical shells. The fact that, when excited, this physical phenomenon is very strong, together with the high resolution and array gain achieved through SAS processing allowed to enhance the image features to such an extent that very accurate verification with the model was possible.

The physics-based interpretation of these features may be a valuable aid to ATR algorithms applied to high-frequency sonar images. Furthermore, once an object is detected from its diffraction highlight (and shadow), but its classification through standard ATR algorithms results uncertain, it might be useful to survey again the seabed area, in such a way to insonify the object at an angle of incident that will excite one of the possible meridional waves, if the object is a liquid-filled cylinder, made for example of steel.

ACKNOWLEDGMENTS

The authors wish to acknowledge D. Brown and D. Cook from NSWC-PC for useful discussions on SAS processing and for providing the AUV sonar data. Many thanks go to A. Bellettini and R. Hollett who developed the SAS processing method applied to the HF sonar data. The FEM-BEM model used to simulate the low-frequency multiple aspect target strength of the cylinder was developed by J. Fawcett. The authors are also grateful to A. Maguer and H. Schmidt, scientists in charge of the MCG'97 and GOATS'98 sea campaigns, respectively, and to all the NURC personnel who contributed to the success of the sea trials mentioned in the paper.

REFERENCES

1. R. Manning, Small object classification performance of high-resolution imaging sonars as a function of image resolution, in Procs. of IEEE Oceans'02, Vol. 4, 2156-2163, 2002.

2. A. Bellettini, *et al.*, Experimental results of a 300 kHz shallow water synthetic aperture sonar, in Procs. of UAM'07 Conf., Crete, 2007.
3. H. Schmidt, *et al.*, GOATS'98 – Bistatic seabed scattering measurements using autonomous underwater vehicles, SACLANTCEN Report SR-302, La Spezia, 1998.
4. A. Tesei, *et al.*, Physics-based detection of man-made elastic objects buried in high-density-clutter areas of saturated sediments, Applied Acoustics, invited to Special Issue on The detection of buried marine targets, 2008 (in press).
5. S.F. Morse, *et al.*, High-frequency backscattering enhancements by thick finite cylindrical shells in water at oblique incidence: Experiments, interpretation, and calculations, J. Acoust. Soc. Am., Vol. 103 (2), 785-794, 1998.
6. S.F. Morse and P.L. Marston, Meridional ray backscattering enhancements for empty truncated tilted cylindrical shells: Measurements, ray model, and effects of a mode threshold, J. Acoust. Soc. Am., Vol. 112 (4), 1318-1326, 2002.
7. S.S. Dodd, Sonar imaging of elastic fluid-filled cylindrical shells, Ph.D. Thesis, ARL:UT Austin, 1995.
8. G. Kaduchak *et al.*, Elastic wave contributions in high-resolution acoustic images of fluid-filled, finite cylindrical shells in water, J. Acoust. Soc. Am., Vol. 100 (1), 64-71, 1996.
9. D. Brown, *et al.*, Results from a small synthetic aperture sonar, Procs. IEEE Oceans Conf., Boston, 2006.
10. A. Maguer, *et al.*, Buried mine detection and classification (Research Summary 1996-1999), SACLANTCEN Report SR-315, La Spezia, 1999.
11. A.D. Pierce and H.-G. Kil, Elastic wave propagation from point excitations on thin-walled cylindrical shells, J. of Vibration and Acoustics, Vol. 112, 399-406, 1990.
12. H. Überall, Acoustics of shells, Acoust. Physics, Vol. 47 (2), 115-139, 2001.
13. A. Tesei, *et al.*, Target parameter estimation using resonance scattering analysis applied to air-filled, cylindrical shells in water, J. Acoust. Soc. Am., Vol. 108 (6), 2891-2900, 2000.
14. M. de Billy, *et al.*, Ray theory applied to the internal caustic identification of liquid cavities acoustically insonified, J. Acoust. Soc. Am., Vol. 95 (2), 1143-1146, 1994.
15. P.L. Marston and D.S. Langley, Glory and rainbow enhanced acoustic backscattering from fluid spheres: Models for diffracted axial focusing, J. Acoust. Soc. Am., Vol. 73 (5), 1464-1475, 1983.
16. N.D. Veksler, Resonance acoustic spectroscopy, Springer, Berlin 1993.
17. J.D. Achenbach, Wave propagation in elastic solids, Elsevier, Amsterdam 1975.
18. G.S. Sammelmann, *et al.*, The acoustic scattering by a submerged spherical shell. I. The bifurcation of the dispersion curve for the spherical antisymmetric Lamb wave, J. Acoust. Soc. Am., Vol. 85, 114-124, 1989.
19. A. Tesei, *et al.*, Verification of a 3-D structural-acoustic finite-element tool against thin-shell scattering models, Procs of the 7th ECUA Conf., Delft, 431-436, 2004.
20. J. Groen, *et al.*, Shadow enhancement in synthetic aperture sonar using fixed focusing, IEEE J. of Oceanic Eng., accepted for publication.